Supporting Information

Low Off-State Current Density in Vertical Organic Field-Effect Transistors via AgNWs/TiO_2 Interface Modification for Neuromorphic Devices

Huihuang Yang[a], Youshan Bi[a], Yujie Yan[b,*], Cong Liu[a], Yuling Wang[a], Daoqi Fang[a], Shuhui Mu[a], Chunbin Cao[a], Yuan Rao[a], Yaqian Liu,[c] Fangxu Yang[d,*] and Xiumei Wang[a,*]

[a] *School of Engineering, Key Laboratory of Agricultural Sensors, Ministry of Agriculture and Rural Affairs, Anhui Agricultural University, Hefei 230036, China.*

[b] *Fujian Provincial Key Laboratory of Functional Materials and Applications, Xiamen University of Technology, Xiamen 361024, China.*

[c] *School of Electronics and Information, Zhengzhou University of Light Industry, Zhengzhou 450002, China.*

[d] *State Key Laboratory of Advanced Materials for Intelligent Sensing, Key Laboratory of Organic Integrated Circuit, Ministry of Education & Tianjin Key Laboratory of Molecular Optoelectronic Science, Department of Chemistry, School of Science, Tianjin University, Tianjin 300072, China.*

[*] *Corresponding author (emails: yujieyan@xmut.edu.cn; yangfangxu@tju.edu.cn; wangxiumei@ahau.edu.cn)*

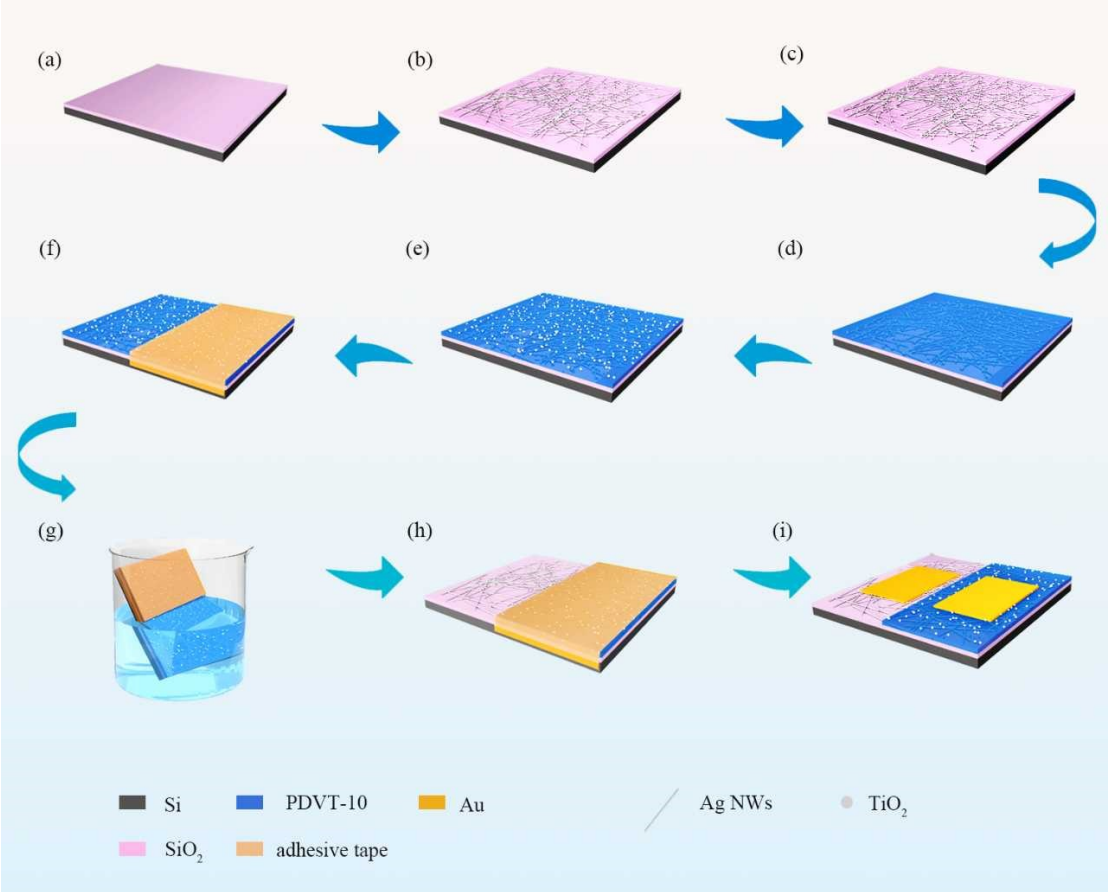

Fig. S1 Schematic diagram of device fabrication process (a) A Si/SiO_2 substrate was cleaned. (b) AgNWs solution was spin-coated and annealed. (c) TiO_2 solution was spray-coated. (d) PDVT-10 solution was spin-coated. (e) TiO_2 solution was spin-coated. (f) The region to be retained was covered with high-temperature tape. (g) Dip the device into the chloroform solution to dissolve the unnecessary part of the mixed film to obtain the exposed source electrode. (h) The PDVT-10/TiO_2 composite film was annealed. (i) Gold source and drain electrodes were thermally evaporated.

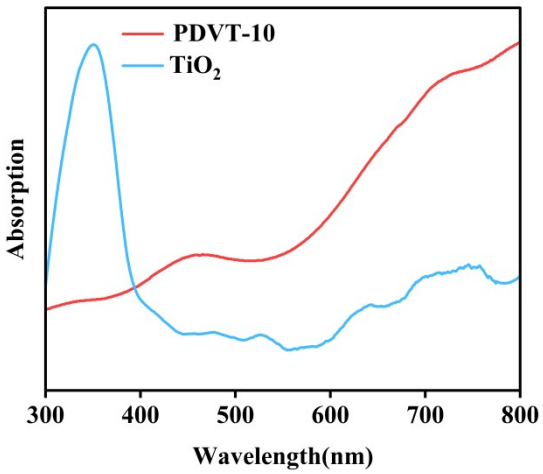

Fig. S2 Absorption spectrum of PDVT-10 and TiO_2 film.

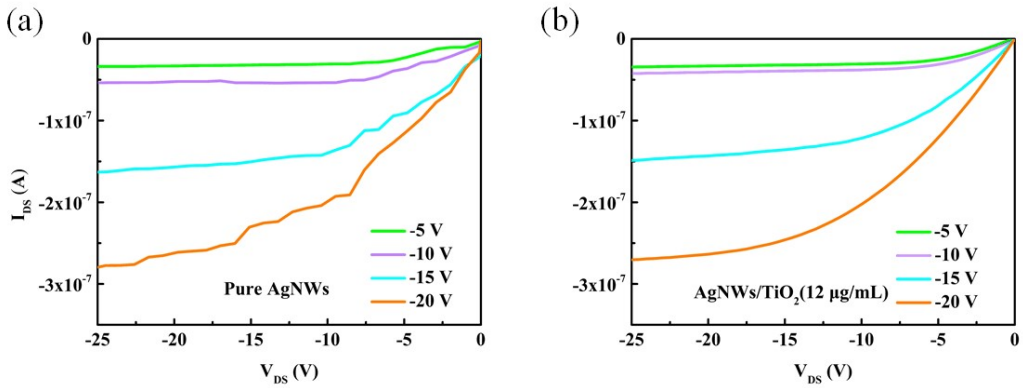

Fig. S3 Output characteristic curves of (a) pure AgNWs-based devices, (b) AgNWs modified with 12 μg/mL TiO_2 devices.

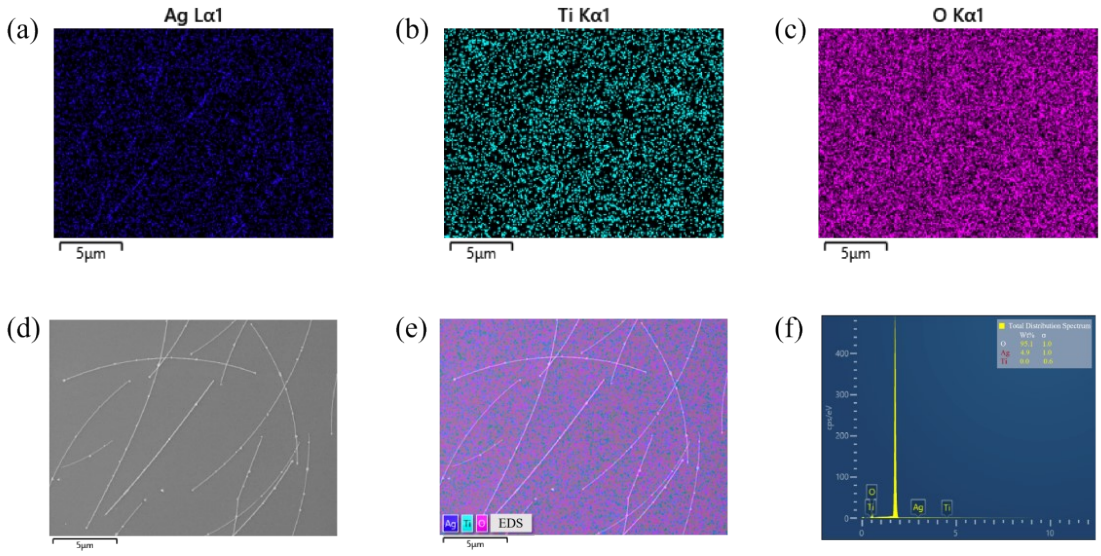

Fig. S4 (a-c) EDS elemental maps of Ag, Ti and O respectively, (d) SEM image of the AgNWs/TiO_2 surface, (e) EDS layered image of AgNWs/TiO_2, (f) EDS spectrum of AgNWs/TiO_2.

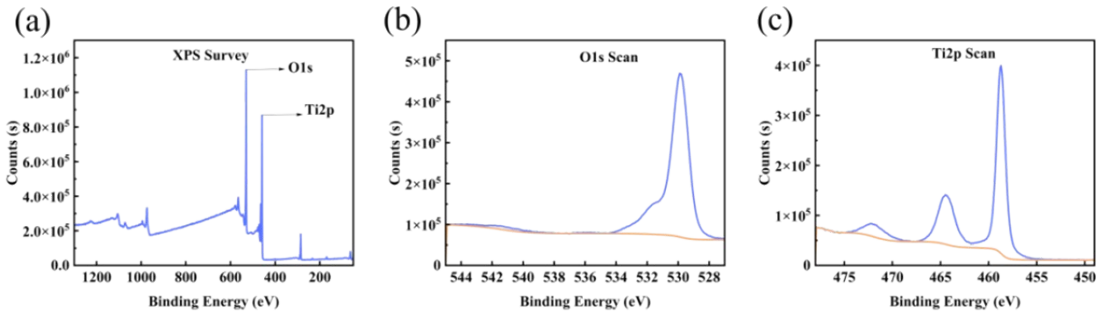

Fig. S5 (a) XPS survey spectrum. (b) High-resolution O 1s spectrum with peak fitting. (c) High-resolution Ti 2p spectrum with peak fitting.

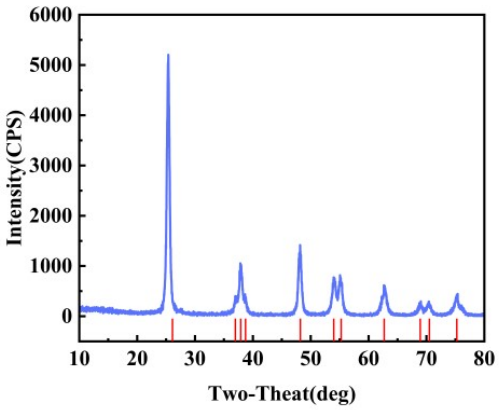

Fig. S6 The XRD pattern of the TiO_2 nanoparticles.

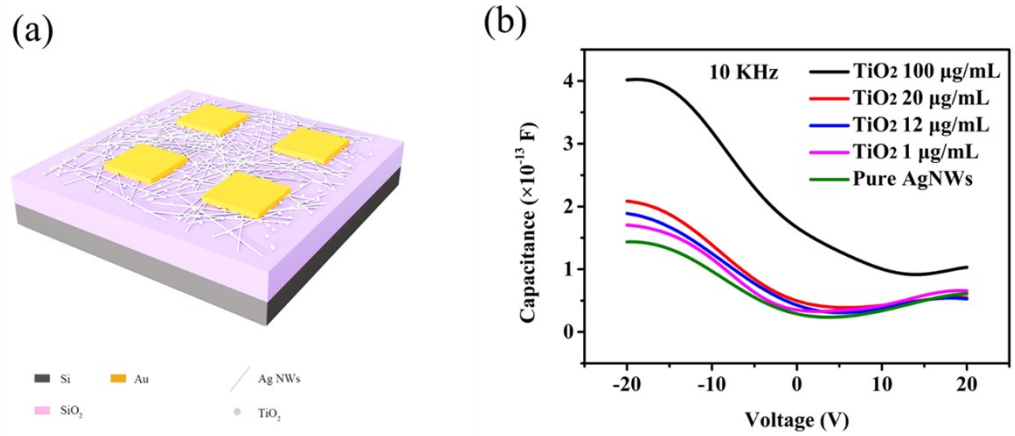

Fig. S7 (a) Device structure diagram for C-V testing. (b) C-V characteristics of devices with different TiO_2 nanoparticle concentrations (0, 1, 12, 20, 100 μg/mL) measured at 10 kHz at room temperature.

Si/SiO_2/AgNW&TiO_2/Au devices were fabricated, as shown in Fig. S7(a), and capacitance-voltage (C-V) measurements were performed. Fig. S7(b) showed the C-V characteristic curves of Si/SiO_2/AgNW&TiO_2/Au devices with different concentrations of TiO_2 nanoparticles sprayed on the AgNW source electrode, measured at a frequency of 10 KHz. All curves exhibited typical C-V behavior of metal-insulator-metal structures: the devices were in the accumulation region under negative bias; as the positive bias increased, the devices entered the depletion region, accompanied by a gradual decrease in capacitance; further increasing the bias led to the inversion region. Compared with pure AgNWs devices, the capacitance of the samples modified with TiO_2 nanoparticles was apparently increased, and the capacitance exhibited an upward trend with the increase of TiO_2 concentration.

The C-V measurement characterized the equivalent series capacitance of the entire metal-insulator-metal structure. For pure silver nanowire devices, AgNWs formed line contact with the SiO_2 surface, resulting in a limited contact area.

Furthermore, the AgNW network contained numerous gaps, which tended to form air gaps (a low-dielectric environment), equivalent to introducing a low-dielectric-constant (Relative Permittivity $\varepsilon_r \approx 1$) air layer between the SiO_2 ($\varepsilon_r \approx 3.9$) and AgNWs. At high frequencies, the equivalent capacitance C_{eq} can be approximately expressed as:

$$\frac{1}{C_{eq}} = \frac{1}{C_{ox}} + \frac{1}{C_{gas}}$$

Wherein: C_{gas} was the capacitance of the air layer, and C_{ox} was the capacitance of the SiO_2 oxide layer. Therefore, the equivalent capacitance under this circumstance was lower than that of the SiO_2 oxide layer. The AgNW source electrode was in direct contact with the organic semiconductor, and the bottom-gate vertical electric field could effectively penetrate into the organic semiconductor layer, which enabled efficient carrier accumulation and regulation of the charge injection barrier, leading to a prominent gate voltage modulation effect.

In contrast, spraying TiO_2 particles onto the AgNWs introduced a dielectric layer with a high relative permittivity ($\varepsilon_r \approx 40\sim60$). This led to an enhancement in the overall equivalent series capacitance, and the equivalent capacitance C_{eq} at high frequencies could be approximately described as:

$$\frac{1}{C_{eq}} = \frac{1}{C_{ox}} + \frac{1}{C_{TiO_2}}$$

Wherein: C_{TiO_2} is the capacitance of the TiO_2 layer.

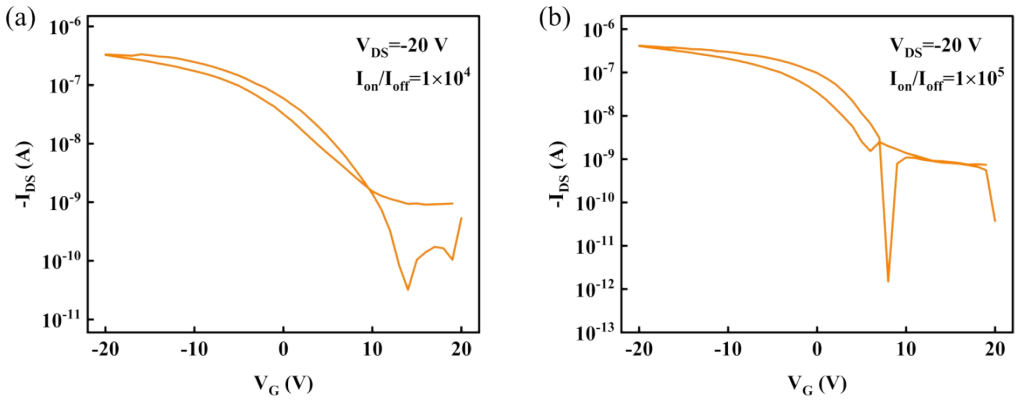

Fig. S8 The corresponding double-sweep hysteresis curves of VOFET devices (a) without and (b) with 12 μg/ml TiO_2 spray-coating on the AgNWs mesh source electrode.

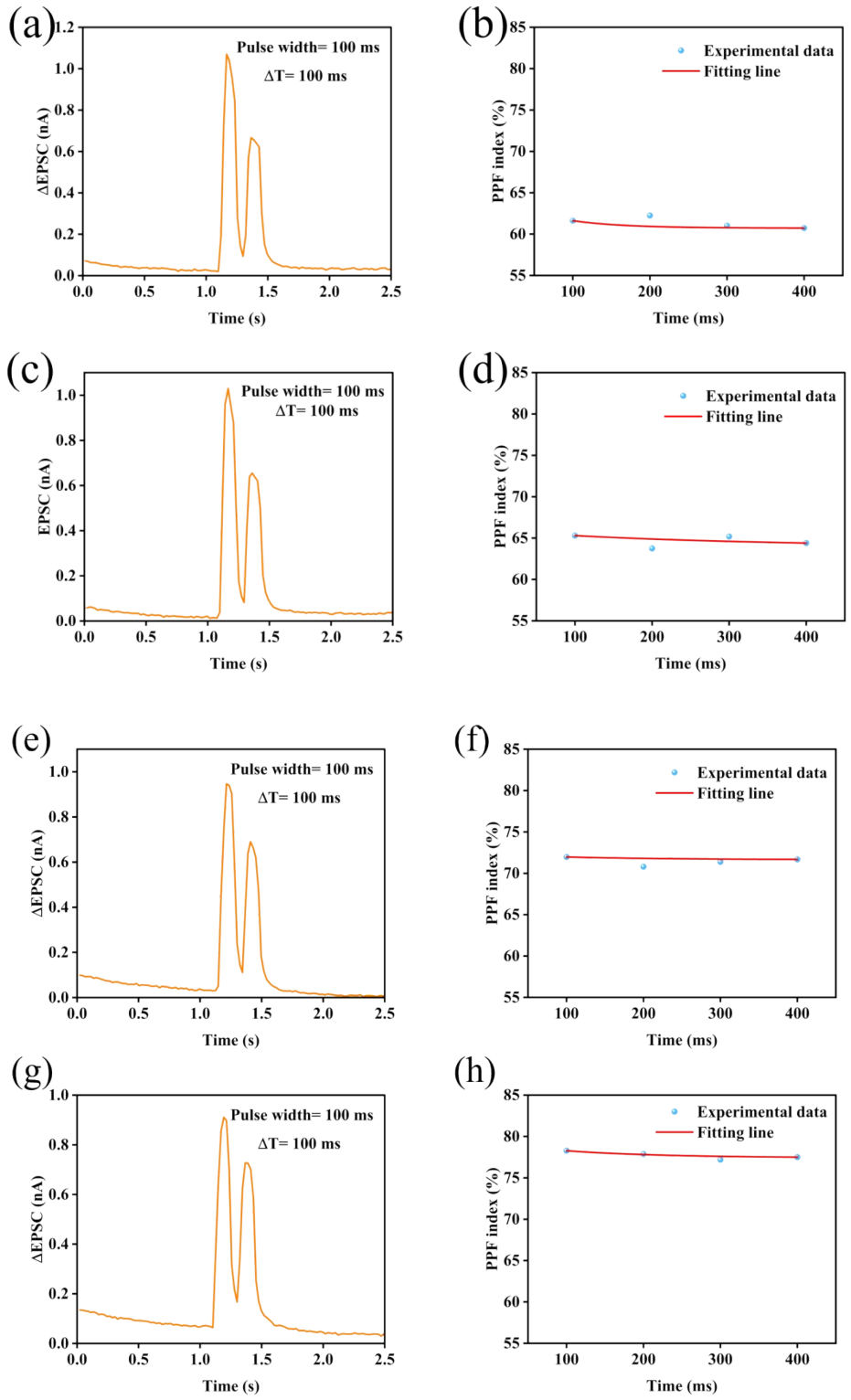

Fig. S9 The EPSC changes under the stimulation of two consecutive optical pulses and the PPF index changes corresponding to VOFET devices with different sprayed concentrations of TiO_2 solutions (a-b) No spraying of TiO_2, (c-d) 1 μg/ml, (e-f) 12 μg/ml, (g-h) 20 μg/ml.

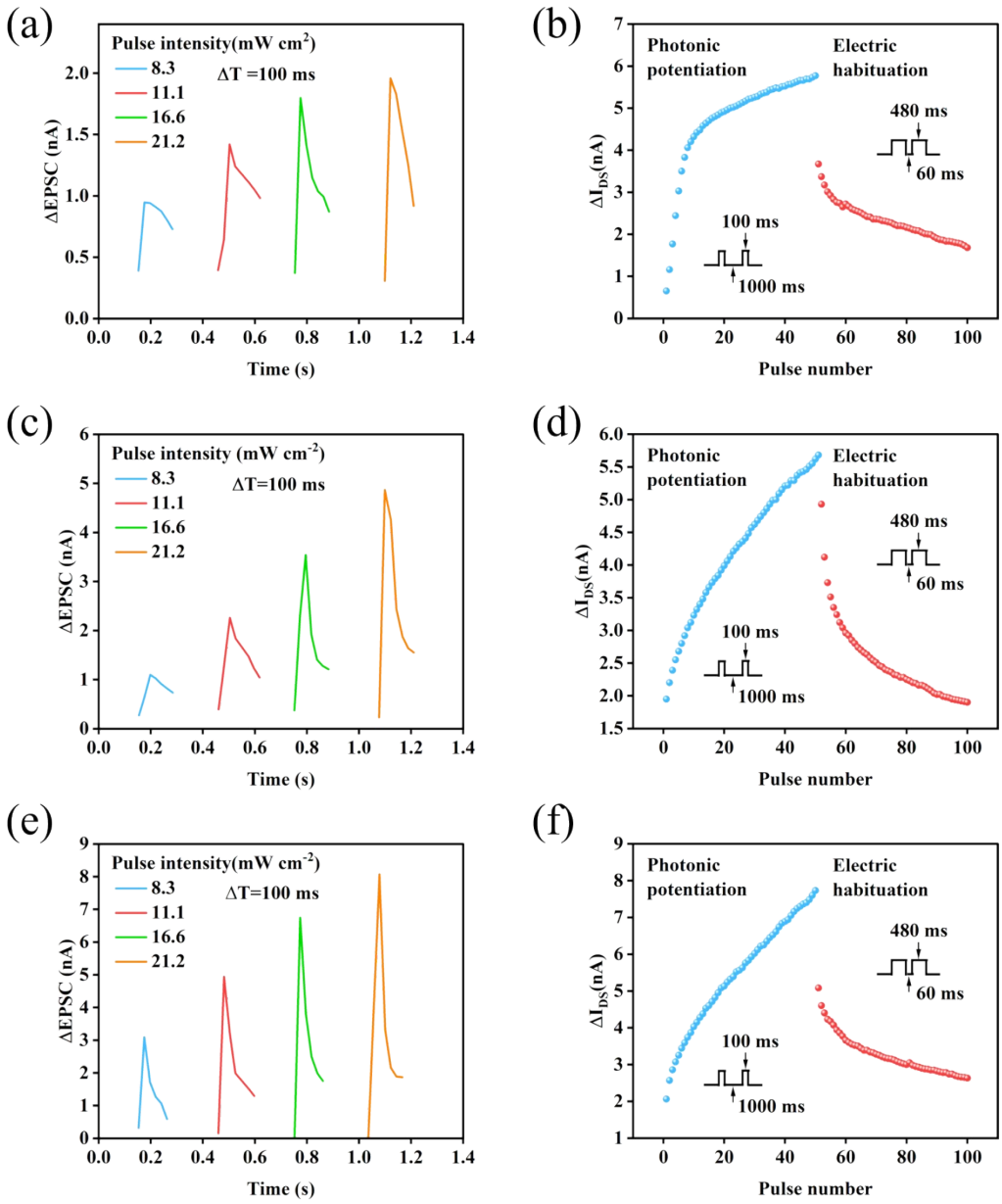

Fig. S10 EPSC changes and multi-level potentiation/depression characteristic curves of neuromorphic devices based on AgNWs&PDVT-10/TiO_2 VOFET by spin-coating TiO_2 layers of different concentrations (a, b) 30 mg/mL, (c, d) 50 mg/mL, and (e, f) 80 mg/mL) onto the PDVT-10 film, respectively.

The EPSC response of AgNWs&PDVT-10/TiO_2 VOFET optoelectronic neuromorphological devices spin-coated with different concentrations of TiO_2 solution under different light pulse

conditions (100 ms pulse width, intensity range 8.3 mW cm^{-2}~21.2 mW cm^{-2}) was presented in Fig. S5(a), (c), (e), respectively. The results indicated that the channel current of the device prepared with 30 mg/mL TiO_2 increased gradually from 1 nA to 2 nA as the light intensity increased, showing a trend toward response saturation. In contrast, devices prepared with 50 mg/mL and 80 mg/mL TiO_2 exhibited stronger photoresponse, while channel currents continued to rise with increasing light intensity without obvious saturation. And the channel currents of the 50 mg/mL and 80 mg/mL devices at the maximum light intensity of 21.2 mW cm^{-2}, reached ~5 nA and ~8 nA, respectively. The LTP and LTD behaviors of VOFET-based devices corresponding to different TiO_2 solution concentrations were illustrated in Fig. S5(b), (d), (f). 50 optical pulses (pulse width: 100 ms, interval: 1000 ms, 4 mW cm^{-2}) followed by 50 electrical pulses (10 V, pulse width 480 ms, interval 60 ms) were applied to investigate the influence of TiO_2 concentration on synaptic LTP/LTD characteristics. The NL values extracted from linear fitting of the LTP/LTD curves were 0.29, 0.078, and 0.12 for the 30 mg/ml device, 50 mg/mL device, and 80 mg/mL device, respectively.

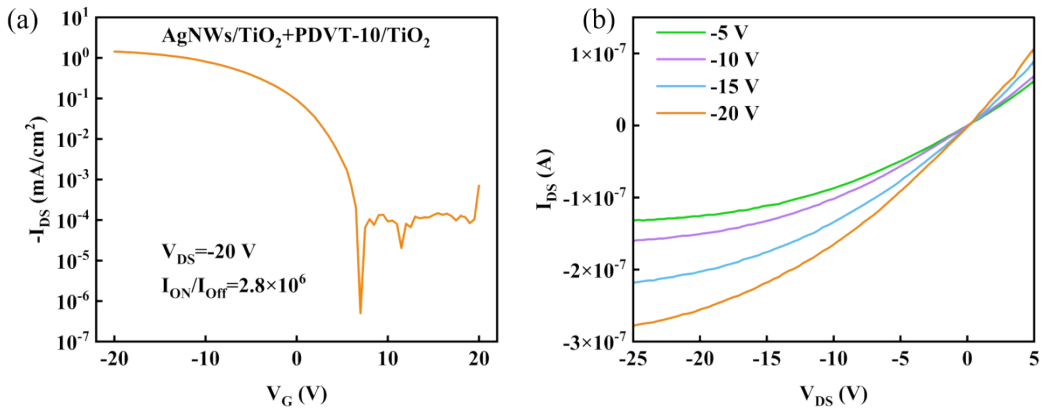

Fig. S11 Transfer and output characteristic curves of AgNWs/TiO_2&PDVT-10/TiO_2 VOFET neuromorphic devices (a) Transfer characteristic curve, (b) Output characteristic curve (Effective channel area, S=200 μm×200 μm).

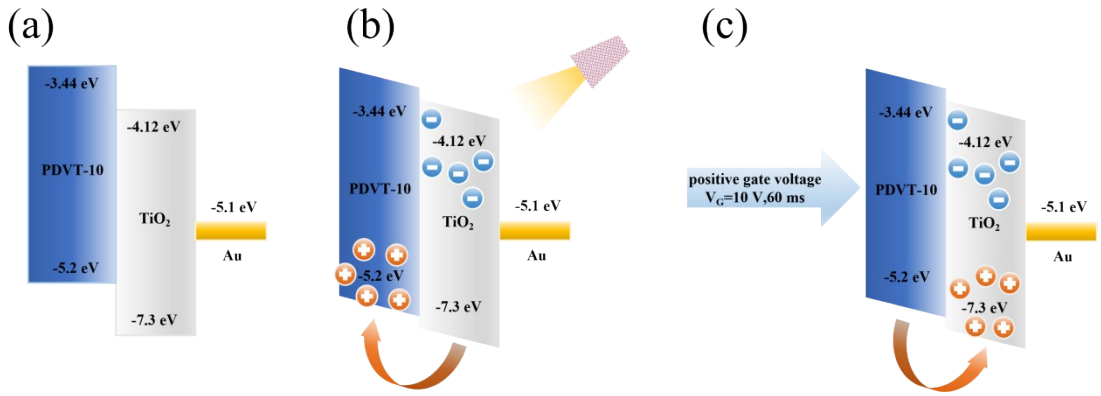

Fig. S12 (a) The device material energy belt structure diagram, The intrinsic mechanism of AgNWs/TiO_2&PDVT-10/TiO_2 VOFET optoelectronic neuromorphic device under (b) optical stimulation and (c) electrical stimulation.

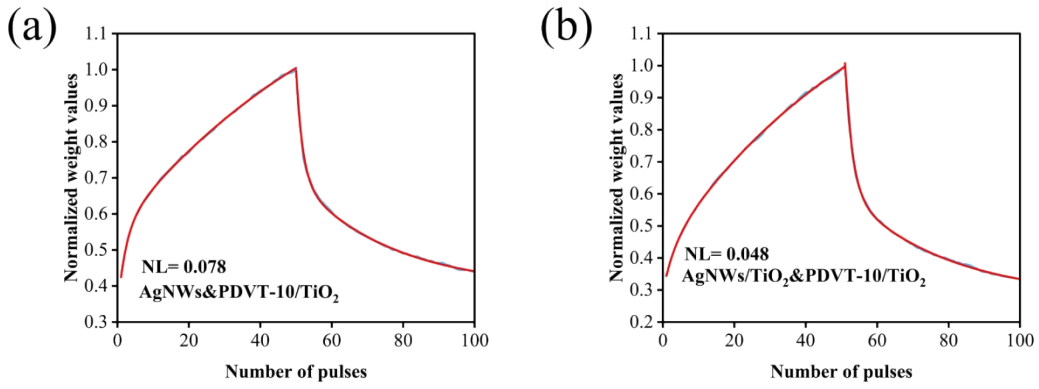

Fig. S13 The normalized weight evolution curve of VOFET optoelectronic neuromorphic devices (a) without spraying, and (b) sprayed with 12 μg/ml TiO_2 solution.

Detailed descriptions of the neural network-based banana ripeness recognition task

Critical parameters for the neural network including dataset split ratio, batch size, learning rate and optimizer were set as follows: the dataset was divided into training set, validation set and test set with the ratio of 88%:8%:4%, corresponding to sample quantities of 11793, 1123 and 562 respectively, with a total of 13478 samples; the batch size was set to 100; the actual device-based learning rate was calculated by the following formula:

$$Learning\ Rate = \frac{B_p + B_d}{2 \times 10^{-6}}$$

$$B_p = \frac{G_{max} - G_{min}}{1 - e^{-A_p}}$$

$$B_d = \frac{G_{max} - G_{min}}{1 - e^{-A_d}}$$

where B_p and B_d were jointly determined by the maximum conductance G_{max}, minimum conductance G_{min} and nonlinear control parameters A_p, A_d of the device; the Adam optimizer was adopted to train the VGG16-based CNN, in which only the learning rate was explicitly configured and adjusted, and other hyperparameters such as momentum adopted the default settings of TensorFlow.

The recognition accuracy on the independent test set reached 93.64%, the corresponding confusion matrix was provided to illustrate the classification performance across different categories, and the training and validation loss curves were also presented to demonstrate the model's convergence behavior during training. The confusion matrix for 4-class classification task was shown in Fig. S14(a). For

each class, the number of correctly classified samples (on the diagonal) was 183 (Class 0), 180 (Class 1), 175 (Class 2), and 180 (Class 3). Minor misclassifications were observed across all categories, with no severe cross-class confusion, indicating that the proposed method performed consistently across all four classes. The training and validation loss curves of the CNN model were shown in Fig. S14(b). Both training and validation losses decreased rapidly in the initial epochs and gradually converge to a low and stable level. No significant divergence or overfitting were observed between the two curves, indicating that the model was well-trained with good generalization ability.

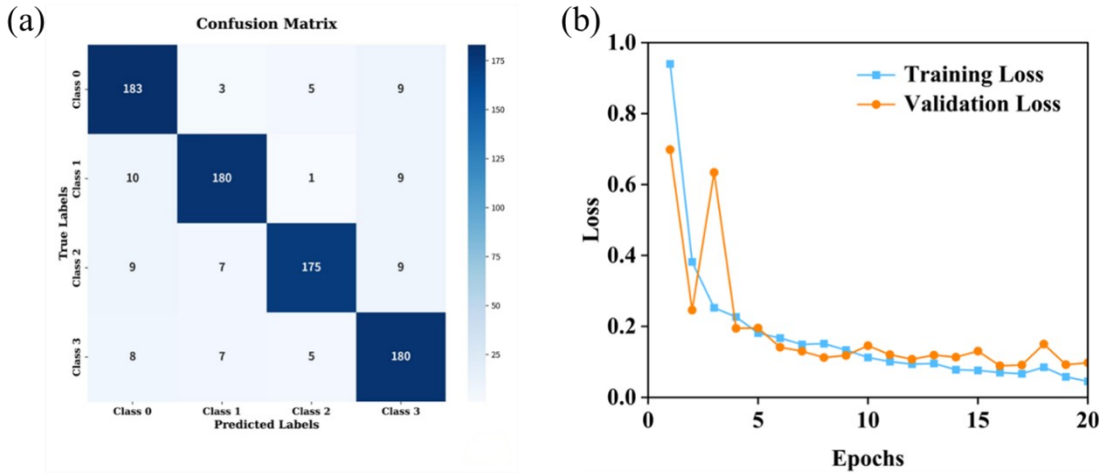

Fig. S14 (a) Confusion matrix for classification results obtained from the test dataset. (b) Training and validation loss curves during model training.

Synaptic weights (W) were the conductance difference between two equivalents synaptic structures, expressed as $W=G_p-G_n$. Here, G_p and G_n were random conductance values uniformly distributed within the range [G_{min}, G_{max}]. Based on the backpropagation algorithm, W increased as G_p increased and decreased as G_n increased. During neural network training, the backpropagation algorithm computed

the theoretical weight update gradient. In hardware simulation, this gradient was converted into specific adjustment commands for the conductances of physical devices G_p and G_n. The conductance change extracted from the "potentiation" and "depression" curves described the detailed information of the synaptic weight change (Fig. 4(g)).